

An Adjoint-Based Aerodynamic Shape Optimization Methodology for Fairing Systems

M. R. Colonna¹, F. Palacios¹, T. Economou², A. K. Lonkar², and J. J. Alonso³
Stanford University, Dept. of Aeronautics & Astronautics, Stanford, CA, 94305

The optimization of a fairing system is formulated in terms of the overall performance of the launch vehicle-fairing system as measured by the total velocity increment within a maximum load constraint at the fairing-vehicle interface. This objective requires a time-accurate treatment of the vehicle's aerodynamics and, when adjoint sensitivities are used for gradient information, a time-accurate adjoint functional as well. The fairing's geometry is parameterized in terms of a local spherical coordinate system which can be perturbed via the manipulation of spline control points or Hicks-Henne bump functions. The local surface perturbation and the continuous adjoint capabilities of the SU² design suite allow for accurate sensitivities of the aerodynamic performance to the geometric parameters for use with gradient-based optimization algorithms. A sample medium-lift launch vehicle is used as an example to demonstrate the method and results of the optimization presented in addition to possibilities to improve the method.

Nomenclature

A	= area
\mathbf{A}	= matrix of linear constraints
$\vec{\mathcal{A}}$	= inviscid flux Jacobian matrices
\mathbf{b}	= vector of linear constraint values
\mathbf{c}	= vector of nonlinear constraint
C_A	= aerodynamic axial force coefficient
C_M	= aerodynamic moment coefficient
C_N	= aerodynamic normal force coefficient
D	= drag force
d	= composite core thickness or beam cross-section measure
\vec{d}	= force projection vector
E	= total energy per unit mass
F_{ale}	= convective fluxes in arbitrary Langrangian-Eulerian form
F_A	= axial force
F_N	= normal force
g_0	= standard Earth gravity
H	= stagnation enthalpy
I_{sp}	= specific impulse
i, j	= indices
J	= objective function
j_S	= scalar function defined on surface S
L	= length
m	= mass
\vec{n}	= unit normal vector
p	= static pressure
q	= dynamic pressure

¹ Engineering Research Associate, Department of Aeronautics & Astronautics, Stanford University, AIAA Senior Member.

² Ph.D. Candidate, Department of Aeronautics & Astronautics, Stanford University.

³ Associate Professor, Department of Aeronautics & Astronautics, Stanford University, AIAA Senior Member.

R	= radius
$\mathbf{R}(U)$	= system of governing flow equations
S	= solid wall boundary (design surface) or reference area
t_0	= initial time
t_f	= final time
\bar{U}	= vector of conservative variables
\vec{u}_Ω	= control volume boundary velocity
V_∞	= free stream velocity
\vec{v}	= flow velocity vector in inertial frame
x	= axial direction
\mathbf{x}	= vector of design variables
α	= angle of attack
β	= side-slip angle
ρ	= density
ρ_∞	= free-stream density
$\vec{\varphi}$	= flow adjoint velocity vector
Γ	= domain boundary
ψ	= vector of flow adjoint variables
Ω	= problem domain
σ	= stress
γ	= ratio of specific heats
$\nabla(\cdot)$	= gradient operator
$\nabla \cdot (\cdot)$	= divergence operator
$\partial_n(\cdot)$	= surface-normal gradient operator, $\vec{n}_S \cdot \nabla(\cdot)$
\cdot	= vector inner product
\times	= vector cross product
\otimes	= vector outer product
$\delta(\cdot)$	= first variation

Subscripts

A	= axial direction
bt	= boat tail section property
cyl	= cylindrical section property
E	= Earth
f	= fairing property
fd	= at fairing deployment
M	= moment
N	= normal direction (to axis)
P	= propellant
PL	= payload
S	= structural
v	= vehicle
∞	= ambient or free stream
0	= initial

Superscripts

$1, 2, \dots, n$	= launch vehicle stage
*	= optimal

I. Introduction

OPTIMUM profiles for launch vehicle and missile fairings have been sought since the early days of rocket flight, focusing primarily on the minimization of aerodynamic drag and, in some cases, aerodynamic heating. Ultimately, the performance measure of interest is the flight performance of the vehicle *as a whole* which includes consideration of disciplines beyond aerodynamics. In order to fully capture the performance impact of the fairing design, a multidisciplinary optimization (MDO) is required which captures the interactions of structural loading, aerodynamic stability, and trajectory performance must be included in an integrated fashion. MDO efforts of rocket systems to date have focused primarily on system-level parameters^{3,4,5} (e.g. staging ratio) rather than directly optimizing the physical variables of the vehicle (e.g. length, radius, skin thickness, etc.) while MDO efforts on other aerospace applications^{6,11,12,19,21} have focused on high-fidelity implementation. Some previous work has been done in the area of high-fidelity rocket and fairing optimization⁷ in addition to some recent work surrounding the aerodynamic shape optimization of asymmetric fairings for large and unconventional payload geometries¹.

In order to isolate the aerodynamic shape optimization problem from the full MDO one without omitting important performance trades, constraints were used to bound the aerodynamic loading applied to the rest of the vehicle. This essentially decoupled the launch vehicle and fairing design by reducing the size of the design space available to a full-vehicle MDO. Within the aerodynamic shape optimization sub-problem of a fairing, three key challenges exist that are not typically encountered in most aerodynamic shape optimizations: 1) the ambient conditions are changing rapidly during either ascent or reentry requiring a time-accurate treatment of performance and sensitivities, 2) the fairing's aerodynamic properties have a considerable impact on the loading sustained by the rest of the vehicle which is not directly modeled, and 3) the very broad range of flow regimes encountered. In order to address these challenges in a consistent way for shape optimization, a time-accurate, continuous surface adjoint formulation was used via the SU² suite of aerodynamic design tools^{20,22}. The cumulative aerodynamic performance of fairing system over the relevant portion of a trajectory to atmospheric flight loads was determined, constrained by one-dimensional-equivalent structural limits of the vehicle.

II. Optimization Problem Formulation

In this section the overall performance of the launch vehicle and structural constraints are developed. Launch vehicle optimization is inherently multidisciplinary in nature and some simplifications are made to expose the most important effects of the fairing's aerodynamic performance, mass properties, and structural loading. The general optimization problem statement is

$$\begin{aligned} \text{Minimize: } & J(\mathbf{x}), \\ \text{Subject to: } & \mathbf{c}(\mathbf{x}) \leq 0, \\ & \mathbf{Ax} \leq \mathbf{b}, \end{aligned} \quad (1)$$

where $\mathbf{c}(\mathbf{x})$ denotes any nonlinear constraints and \mathbf{A} denotes a matrix of linear constraint coefficients with corresponding values \mathbf{b} . In the sections below two different objective functions are developed and the nonlinear constraint discussed. The subsequent section discusses the parameterization of the system's geometry and the associated linear constraints. Later sections discuss the sensitivities of J and \mathbf{c} based on a continuous adjoint formulation and detail the optimization procedure itself.

A. Performance

Consider the general multi-stage rocket equation, Eq. (2), with the final stage performance separated from the summation. This famous equation elegantly reveals the system-level parameters key to the performance of any rocket vehicle: 1) propulsion efficiency (I_{sp} , measured in seconds in the formulation below), 2) the mass ratios (full mass to empty) of the stages, 3) the number of stages (n), and 4) the trajectory's losses (ΔV_{losses}) or the deviation from the ideal performance. The loss terms include the velocity increment lost to aerodynamic drag, Eq. (3), and the velocity increment lost to finite-time flight in a gravitational field (ΔV_g). The fairing mass, in essentially all practical systems, is a small fraction of the final stage's initial mass and a very small fraction of the vehicle's initial mass. Equation 2, in the form shown below, implicitly assumes that the fairing is deployed sometime during the final stage flight, separating it into two sub-stages at a specific propellant mass (subscript fd). Evaluating this expression with values of practical systems shows that even for $m_f \rightarrow 0$ the total performance gain expressed in terms of ΔV_{tot} is small. This, however, must be considered in the context of the launch vehicle performance as a whole. For any chemically-powered launch vehicle system, the payload mass fraction (fraction of the liftoff mass that corresponds

to the payload) is very small. Hence, small savings in either m_f or ΔV_{losses} from an optimized fairing are critical due to the high sensitivity of the relevant performance metric, not to mention the cost of access to space.

$$\begin{aligned} \Delta V_{tot} &= \sum_{i=1}^{n-1} I_{sp}^i g_0 \ln\left(\frac{m_0^i}{m_0^i - m_p^i}\right) + I_{sp}^n g_0 \left[\ln\left(\frac{m_S^n + m_P^n + m_{PL} + m_f}{m_S^n + (m_P^n)_{fd} + m_{PL} + m_f}\right) + \ln\left(\frac{m_S^n + (m_P^n)_{fd} + m_{PL}}{m_S^n + m_{PL}}\right) \right] - \Delta V_{losses} \\ m_0^i &= \sum_{j=i}^n (m_S^j + m_P^j) + m_{PL} + m_f \end{aligned} \quad (2)$$

$$\Delta V_{losses} = \Delta V_g + \Delta V_D = \Delta V_g + S \int_{t_0}^{t_f} \frac{q_\infty(t) C_D(t)}{m_v(t)} dt \quad (3)$$

In this study we seek to minimize not the drag force itself nor even the drag force at a finite set of discrete conditions but the functional formed by Eq. (2): an integration of the drag force, the changing ambient conditions, and the changing vehicle mass. This requires a method by which sensitivities can be obtained to functionals varying in time and the continuous adjoint approach used presently is summarized in a subsequent section. In order to isolate the fairing's effects and limit the scope of the problem the vehicle's trajectory was assumed to fixed. While aerodynamic loading can have an impact on the trajectory close to the maximum q_∞ point, its overall impact is minimal and was neglected. This assumption represents a significant simplification but removed the need to recompute the trajectory for each design – a major corresponding reduction in computational cost.

The total velocity increment for a typical low-Earth-orbit mission is ~ 9 km/s. When establishing an objective function for numerical evaluation it is preferable to scale both the objective and variables to $\sim O(1)$. Hence, the objective used here divides the total velocity increment by an orbital velocity scale for Earth,

$$J \equiv -\frac{\Delta V_{tot}}{\sqrt{Gm_E / R_E}}. \quad (4)$$

The negative sign corresponds to minimization consistent with the canonical optimization problem formulation. It must also be noted that the vehicle's drag is only partially accounted for by the fairing. Here we assume that the contribution to the drag of the rest of the vehicle, integrated over the trajectory, is a constant which is independent of the fairing's geometry. Hence, ΔV_D can be expressed as the sum of the fairing's drag and that of the rest of the vehicle. The constant terms merely shift the objective value and do not play a role in optimization.

Finally, sensitivities of the objective function are required. The sensitivity of the ΔV_D functional of Eq. (3) is evaluated directly by SU², discussed in detail in a subsequent section. The remaining terms of Eq. (2) rely upon the mass of the fairing and can hence be expressed as the sensitivity of m_f to the design variables. This is discussed in the mass properties section below.

B. Aerodynamics

Most generally, the aerodynamics of a launch vehicle at a given instant in an ascent trajectory are a function of the current altitude (atmospheric conditions) and velocity in addition to the vehicle's orientation. The latter requires a six-degree-of freedom dynamic analysis involving the instantaneous wind conditions, the vehicle's structural dynamics, and its control system – all of which are beyond the scope of this work. A simplification frequently employed to decouple this tightly-interdisciplinary problem (and provide weather limits for launch) is to rate the vehicle to a maximum $q_\infty \alpha$, or product of dynamic pressure and angle of attack, essentially linearizing the aerodynamics and structural dynamics of the vehicle for small α .

Consistent with the assumption that $q_\infty(t)$ is fixed, maximum $q_\infty(t) \alpha(t)$ is fixed if a value of α at maximum q_∞ is assumed. This adds an additional scalar input to the optimization which defines the maximum aerodynamic loading but does not change the optimization procedure itself. The nominal trajectory, from a performance standpoint, neglects winds and dynamics or, equivalently, assumes $\alpha = 0$ throughout. In order to save the computational expense of evaluating the aerodynamics at both $\alpha = 0$ (for nominal performance) and $\alpha = \alpha_{max}$ (for loads), the lateral and axial force coefficients are assumed to be proportional to $\sin(\alpha)$ and $\cos(\alpha)$, respectively, for small α . Hence, C_A and C_M are evaluated at $\alpha = \alpha_{max}$ only and the nominal ($\alpha = 0$) value of C_A for drag loss is given by

$$C_A(\alpha) = C_A(0)\cos(\alpha) = C_D \cos(\alpha) . \quad (5)$$

Finally, the drag loss due to the fairing is given by

$$\Delta V_{D_f} = S \int_{t_0}^{t_f} \frac{q_\infty(t)}{m_v(t)} C_{A_f}(t; \alpha = 0) dt . \quad (6)$$

C. Structural Load Constraint

Since the fairing, for the purposes of this problem, was designed independent of the launch vehicle on which it would fly, limiting loads at the vehicle-fairing interface must be established a priori. The total load applied to the vehicle was reduced to an equivalent axial force and bending moment at the interface. These include both the contribution of aerodynamic forces and the inertial forces for a given load case defined by an axial acceleration, a_x , dynamic pressure (q_∞), and angle of attack (α). Assuming a thin-walled primary structure, only the axial stress state was considered (shear is neglected). The maximum of these total interface forces must be constrained to ensure the vehicle is not overloaded. Employing a one-dimensional structural model for the vehicle, these were combined to form an *equivalent static line load* at the vehicle-fairing interface, defined in Eq. (9) and simplified through judicious choices of the normalizing area (S) and length (L) for aerodynamic coefficients, Eqs. (7). A representative structural cross-sectional area (A_v) and second moment of area (I_v) for the vehicle primary structure are required parameters. Here, a thin-walled, circular cross-section was assumed for the vehicle and the second moment of area and cross-sectional area estimated via the thin-walled formulation, Eqs. (7). With this substitution, a characteristic wall thickness (d_v) replaces the parameter I_v . Finally, a reference stress for the vehicle primary structure material(s) (σ_{ref}) is required for comparison to the line loads. In summary,

$$S = \pi R_v^2 , I_v \approx \pi R_v^3 d_v , A_v \approx 2\pi R_v d_v , \quad (7)$$

$$C_A \equiv \frac{F_A}{q_\infty S} , C_M \equiv \frac{M}{q_\infty S R_v} , \quad (8)$$

$$C_{load_f} \equiv \frac{1}{\sigma_{ref}} \left(\frac{F_A + m_f a_x}{A_v} + \frac{MR_v}{I_v} \right) = \frac{q_\infty R_v}{\sigma_{ref} d_v} \left(\frac{1}{2} C_A + C_M \right) + \frac{m_f a_x}{2\pi R_v d_v \sigma_{ref}} . \quad (9)$$

Lateral inertial loads, which are primarily a function of vehicle structural dynamics, have been neglected. In similar fashion to the drag losses above, C_{load} is taken to be the loads applied to the vehicle from the fairing's aerodynamic loading only and not a representation of the total static or dynamic loading on the vehicle (which is considerably more complex). Returning to the context of the optimization problem, C_{load} must be \leq its maximum allowable value for the vehicle, an additional scalar parameter, acting as a nonlinear constraint.

D. Mass Properties

The final aspect of Eq. (2) requiring consideration is the mass of the fairing. Without a detailed structural design the internal structure of the must remain constant with respect to changes in the design variables (though it can be an a priori function of position) and the mass of the fairing is simply a function of the fairing's surface area – a major simplification. This essentially requires the fairing's internal structure to be overdesigned and neglects any additional gains in performance possible through an aero-structural optimization. Here, the surface density distribution (mass per unit area) of the fairing's skin is an input parameter. This density can include both structural and non-structural mass, averaged over the surface area.

With this distribution, the fairing's mass can be evaluated by integrating over the surface area in a spherical coordinate system. If the fairing's surface is specified as $r(\theta, \phi)$ its mass is given by

$$m_f = \int_0^{2\pi} \int_{\pi/2}^0 \sigma_s(\theta, \phi) r_f(\theta, \phi)^2 \sin(\theta) d\phi d\theta , \quad (10)$$

where θ is the polar angle from the nose and ϕ is the azimuth (see Fig. 2 and subsequent section for detailed discussion of geometry). For an axisymmetric fairing only the distribution in θ is required,

$$m_f = 2\pi \int_0^{\pi/2} \sigma_s(\theta) r_f(\theta)^2 \sin(\theta) d\theta. \quad (11)$$

If the geometry is parameterized in $r(\theta, \phi)$ the sensitivities of m_f to the design parameters can be evaluated directly from Eq. (10) or Eq. (11). While analytical sensitivities are possible for sufficiently simple $r(\theta, \phi)$, a complex step method was used here for general application to any parameterization, yielding the sensitivities $\partial m_f / \partial x_i$.

III. Geometry & Grid Deformation

A nominal EELV-sized^{17,24} payload fairing (of similar shape and scale that of a ULA Delta II²³) is shown in Fig. 1. This fairing includes a flair-down or “boat tail” region aft of the payload compartment allowing for payload diameters which are greater than the vehicle’s diameter. The payload volume and dynamic envelope (R_{PL} and L_{cyl}) were assumed fixed by satellite needs resulting in a volume constraint on the fairing’s shape. The curved portion of the fairing is typically a spline or otherwise-parameterized curve tangent at either end to the cylindrical section of the fairing and a normal to the axis of rotation at the nose.

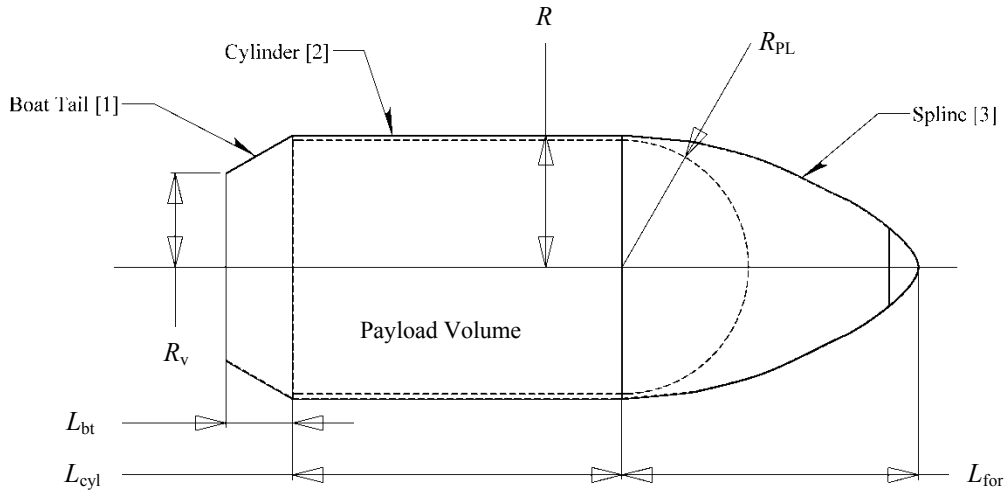


Figure 1. Cross-sectional view of nominal fairing design. Dotted line shows payload volume envelope.

An axisymmetric geometry is shown in Fig. 1 and is used as the sample case in this study, though the optimization method applies to any general geometry of the form $r(\theta, \phi)$. Due to the payload constraints mentioned above, only the forward region is parameterized and considered for optimization. Any parameterization that can produce the profile of the fairing, $r(\theta, \phi)$ or $r(\theta)$ for axisymmetric geometries, can be accommodated within the current framework. Here, two approaches were considered: 1) A cubic spline interpolant of m control points $\{\theta_i, r_i\}$ (tensor product spline surface with control points $\{\theta_i, \phi_i, r_i\}$ for general surfaces) and $dr/d\theta = 0$ boundaries to provide the proper tangency. 2) A set of Hicks-Henne bump functions at m control points $\{\theta_i, \Delta r_i\}$ which are added to the baseline surface. The general parameterization of the geometry is depicted in Fig 2.

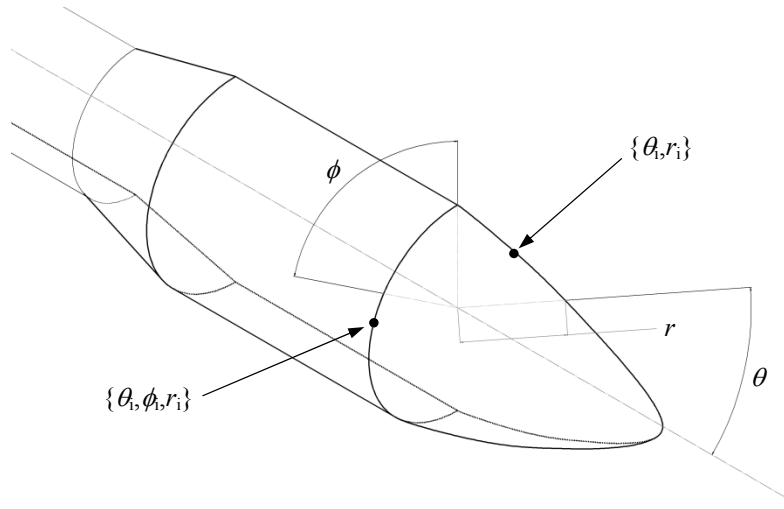


Figure 2. General parameterization of the fairing nose geometry and control points.

In order to allow movement of the nose point when using Hicks-Henne functions^{14,25}, a modification is required at the nose. Defining the Hicks-Henne independent variable, $u \in [0 \rightarrow 1]$, as

$$u(\theta) \equiv 2 \frac{\theta}{\pi}, \quad (12)$$

the general Hicks-Henne function in this application takes the form

$$\begin{aligned} f_i(r) &= \Delta r_i \left[\sin(\pi u^{n_i}) \right]^{p_i}, \\ n_i &= \frac{\log_{10}(0.5)}{\log_{10}(u_i)}. \end{aligned} \quad (13)$$

The amplitude (Δr^i), peak location (u_i), and width (p_i) are all design parameters. Hicks-Henne functions, by construction, go to zero at $u = 0$ and $u = 1$ and hence no function could be placed at the nose ($u = 0$). To circumvent this at the nose the definition is modified slightly to capture only half of the function ($0.5 < u < 1.0$):

$$\begin{aligned} u_{nose} &= 0.5, \\ u(\theta) &= \frac{\theta}{\pi} + 0.5. \end{aligned} \quad (14)$$

With the modification above the nose can be smoothly stretched independently. This new set of partially-modified Hicks-Henne functions provides a means to smoothly deform the baseline surface to an arbitrary level of detail.

With the outer surface of the fairing parameterized, care must be taken in the form of constraints to ensure valid geometries. Allowing geometries with inherently poor performance may impede converge of the optimization but will not result in errors. Here, we seek only to eliminate invalid geometries. First we seek to eliminate any surface that crosses the axis of rotation:

$$\min[r(\theta, \phi)] > 0. \quad (15)$$

When using spline interpolation, enforcement of this constraint requires some detail. Even if all the control points are taken to have $r_j > 0$ the interpolated values between them (especially for higher-order polynomials basis functions and a small number of control points) can still become negative. Hence, the minimum r must be found in each segment of the spline, resulting in a more complex statement of the constraint,

$$\min[r(\theta, \phi; r_j, r_{j+1})] > 0 \quad \text{for } j = 1, \dots, m-1. \quad (16)$$

Hicks-Henne functions are similar: the new profile formed by the sum of the baseline and all the Hicks-Henne functions must have positive radius everywhere,

$$\min \left[r_0(\theta, \phi) + \sum_{i=1}^m f_i(\theta, \phi) \right] > 0. \quad (17)$$

Finally, we prevent any profiles which form an angle with the axis of rotation greater than normal. In other words, the fairing surface should be normal to the axis of rotation at the nose only and have an angle of incidence everywhere else between normal and zero:

$$\tan^{-1} \left(\frac{r(\theta, \phi)}{\partial r(\theta, \phi) / \partial \theta} \right) \leq \frac{\pi}{2}. \quad (18)$$

Surfaces with reward-facing portions are permitted though will likely perform poorly. This completes the parameterization of the geometry and its corresponding constraints. Collectively, these constraints will be referred to “geometric constraints” throughout the remainder of this work.

The parameterizations discussed above only define points on the fairing surface. In order to modify the aerodynamic model (details below in a subsequent section) the volume mesh must be deformed in a way that does not produce cells which are inverted or of very poor quality. This is of particular importance, from a practical matter, in optimization applications where a potentially-large number of designs will be evaluated in an automated fashion. Hence, cells which cause either divergence in the flow solver or locally inaccurate results can disrupt an optimization in ways that are not always easy to detect. Here, we use a spring analogy deformation algorithm, similar to that of Ref. (8), which treats the edges of cells as linear “springs” which resist deformation. The new surface coordinates act as a displacement boundary condition and the equilibrium position of the volume nodes is solved for.

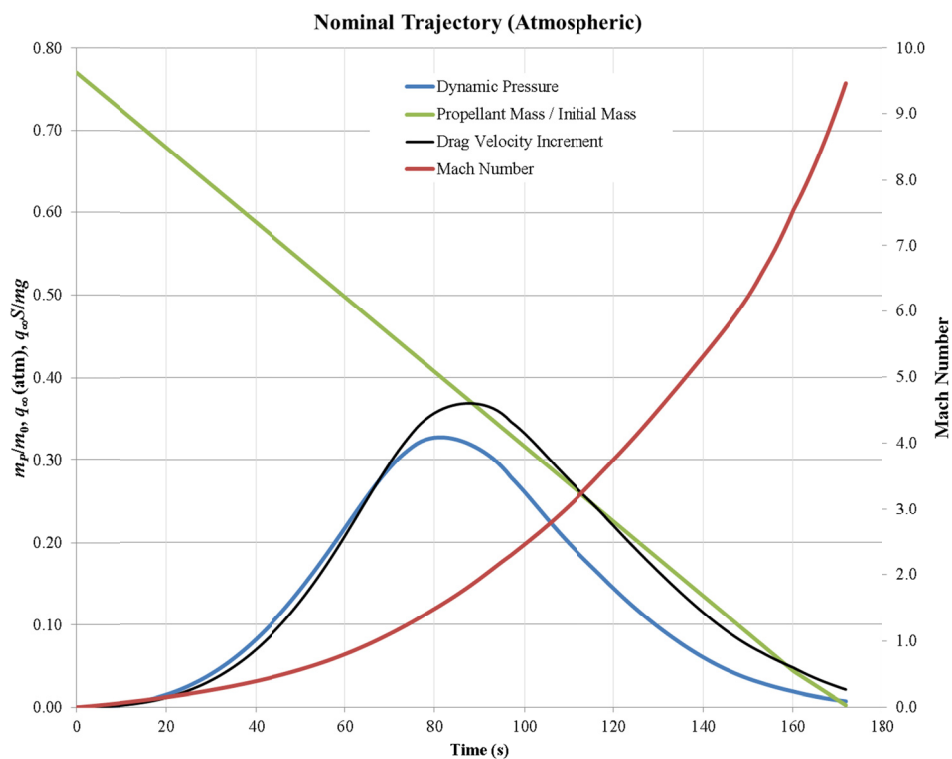


Figure 3. Selected data from nominal ascent trajectory. Note that the integrand of the drag velocity increment is biased toward higher Mach number range of flight due to the decreasing mass.

IV. Nominal Trajectory

A nominal trajectory to 185 km circular orbit was computed corresponding to the baseline vehicle (summarized below) and fairing yielding $q_\infty(t)$, $M(t)$, $m(t)$, and the transient free stream conditions required for CFD analysis. A Standard Atmosphere model was used. The atmospheric portion of the trajectory used in this study is plotted above in Fig. 3. Cubic spline interpolation was used between the trajectory data point where necessary to generate free stream conditions.

V. Governing Flow and Adjoint Problems for Unsteady Aerodynamics

The SU² suite of tools^{20,22} was utilized for flow and adjoint solutions¹⁵, including a time-accurate adjoint formulation allowing for the evaluation of the drag loss functional in Eq. (2). SU² features an unstructured flow solver and continuous adjoint formulation for surface sensitivities to aerodynamic properties. This section contains a summary of the governing flow equations and corresponding time-accurate continuous adjoint formulation for aerodynamic analysis and design.

A. Description of the Physical Problem

Ideal fluids are governed by the Euler equations. In our particular problem, these equations are considered in a domain, Ω , bounded by a disconnected boundary which is divided into a far-field component, Γ_∞ , and a solid wall boundary, S , as seen in Fig. 4. The surface S will also be referred to as the design surface and it is considered continuously differentiable (C^1). Normal vectors to the boundary surfaces are directed out of the domain by convention.

We are interested in time-accurate fluid behavior around aerodynamic bodies in arbitrary motion for situations where viscous effects can be considered negligible. The governing flow equations in the limit of vanishing viscosity are the compressible Euler equations, and these conservation equations can be expressed in arbitrary Lagrangian-Eulerian differential form as

$$\begin{aligned} \frac{\partial \vec{U}}{\partial t} + \nabla \cdot \vec{F}_{ale} &= 0 && \text{in } \Omega \\ (\vec{v} - \vec{u}_\Omega) \cdot \vec{n}_S &= 0 && \text{on } S \\ W_{\Gamma_\infty}^+(\vec{U}) &= W_\infty && \text{on } \Gamma_\infty, \end{aligned} \quad (19)$$

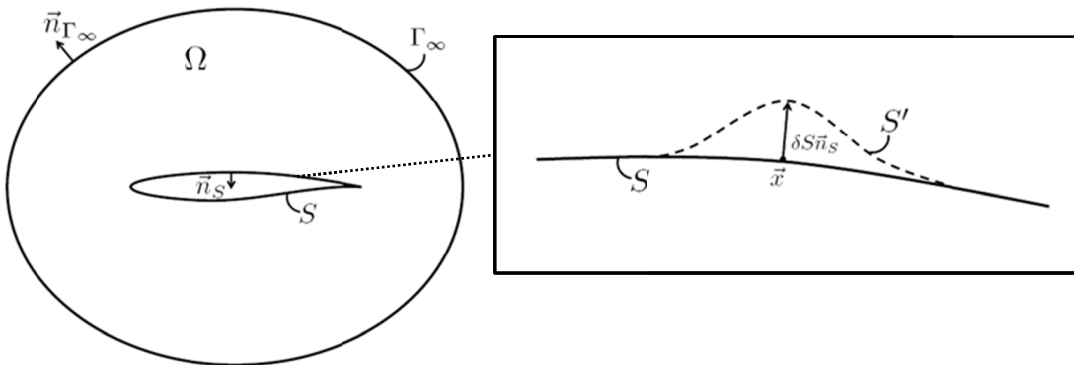


Figure 4. Schematic of volume and surface domains for the continuous adjoint formulation with surface shape perturbation.

where

$$\vec{U} = \begin{Bmatrix} \rho \\ \rho \vec{v} \\ \rho E \end{Bmatrix}, \vec{F}_{ale} = \begin{Bmatrix} \rho(\vec{v} - \vec{u}_\Omega) \\ \rho \vec{v} \otimes (\vec{v} - \vec{u}_\Omega) + \bar{\bar{I}} p \\ \rho E(\vec{v} - \vec{u}_\Omega) + p \vec{v} \end{Bmatrix}, \quad (20)$$

ρ is the fluid density, $\vec{v} = \{u, v, w\}^T$ is the flow velocity, \bar{u}_Ω is the local velocity for a domain in motion, E is the total energy per unit mass, and p is the static pressure. (In the present application, \bar{u}_Ω is zero.) The second line of Eqs. (19) represents the flow tangency condition at a solid wall. The final line represents a characteristic-based boundary condition at the far-field where, in general, the fluid states at the boundaries are updated depending on the sign of the eigenvalues. The boundary conditions take into account any boundary velocity due to control volume motion. In order to close the system of equations after assuming a perfect gas, the pressure is determined from

$$p = (\gamma - 1)\rho \left[E - \frac{1}{2}(\vec{v} \cdot \vec{v}) \right], \quad (21)$$

and the stagnation enthalpy is given by

$$H = E + \frac{p}{\rho}. \quad (22)$$

B. Surface Sensitivities via a Time-Accurate Continuous Adjoint Approach

The objective of this section is to describe the way in which we quantify the influence of geometric modifications on the pressure distribution at a solid surface in the flow domain.

A typical shape optimization problem seeks the minimization of a certain cost function, J , with respect to changes in the shape of the boundary, S . Therefore, we will concentrate on functionals defined as time-varying quantities on the solid surface S ,

$$J = \int_{t_0}^{t_f} \int_S j_S ds dt, \quad (23)$$

where j_S is a time-dependent scalar function defined at each point on S .

Therefore, the goal is to compute the variation, or change, of Eq. (23) caused by arbitrary but small (and multiple) deformations of S and to use this information to drive our geometric changes in order to find an optimal shape for the design surface, S . This leads directly to a gradient-based optimization framework. The shape deformations applied to S will be infinitesimal in nature and can be described mathematically by

$$S' = \{\vec{x} + \delta S(\vec{x})n_S(\vec{x}), \vec{x} \in S\}, \quad (24)$$

where S has been deformed to a new surface S' by applying an infinitesimal profile deformation, δS , in the local normal direction, \vec{n}_S , at a point, \vec{x} , on the surface, as shown above in Fig. 4.

Surface shape deformations will result in variations of the pressure distribution along the surface, so we will focus on pressure-based functionals with the form

$$j_S = \vec{d} \cdot (p\vec{n}_S). \quad (25)$$

The vector \vec{d} is the force projection vector, and it is an arbitrary, constant vector which can be chosen to relate the pressure, p , at the surface to a desired quantity of interest. For aerodynamic applications, example candidates are

$$\begin{aligned} C_D: \quad & \vec{d} = (\cos \alpha \cos \beta, \sin \alpha \cos \beta, \sin \beta) / C_\infty, \\ C_L: \quad & \vec{d} = (-\sin \alpha, \cos \alpha, 0) / C_\infty, \\ C_{SF}: \quad & \vec{d} = (-\sin \beta, \cos \alpha, -\sin \beta \sin \alpha, \cos \beta) / C_\infty, \\ C_L/C_D: \quad & \vec{d} = \frac{1}{C_\infty C_D} \left(-\sin \alpha - \frac{C_L}{C_D} \cos \alpha \cos \beta, -\frac{C_L}{C_D} \sin \beta \cos \alpha - \frac{C_L}{C_D} \sin \alpha \cos \beta \right), \end{aligned} \quad (26)$$

where $C_\infty = \rho_\infty V_\infty^2 A / 2$, V_∞ is the free stream velocity, ρ_∞ is the free stream density, and A is a reference area.

The minimization of Eqn. (19) can be considered a problem of optimal control whereby the behavior of the governing flow equation system is controlled by the surface shape with deformations of the surface acting as the control input. Furthermore, any variations of the flow variables due to surface deformations are constrained to satisfy the system of governing flow equations,

$$\mathbf{R}(\vec{U}) = \frac{\partial \vec{U}}{\partial t} + \nabla \cdot \vec{F}_{ale} = \frac{\partial \vec{U}}{\partial t} + \nabla \cdot \vec{F} - \nabla \cdot (\vec{U} \otimes \vec{u}_\Omega) = 0, \quad (27)$$

where the terms involving the control volume motion have been separated from the traditional Euler fluxes. Mathematically, the constrained optimization problem can be formulated as follows:

$$\begin{aligned} \text{Minimize } J &= \int_{t_0}^{t_f} \int_S \vec{d} \cdot (p \vec{n}_S) ds dt \\ \text{Such that } \mathbf{R}(\vec{U}) &= 0 \end{aligned} \quad (28)$$

Following the adjoint approach to optimal design, the constrained optimization problem in Eq. (28) can be transformed into an unconstrained optimization problem by adding the inner product of an unsteady adjoint variable vector, ψ , and the governing equations integrated over the domain (space and time) to form the Lagrangian:

$$J = \int_{t_0}^{t_f} \int_S \vec{d} \cdot (p \vec{n}_S) ds dt + \int_{t_0}^{t_f} \int_\Omega \Psi^T \mathbf{R}(\vec{U}) d\Omega dt, \quad (29)$$

where we have introduced the adjoint variables, which operate as Lagrange multipliers and are defined as

$$\Psi = \begin{Bmatrix} \psi_\rho \\ \psi_{\rho u} \\ \psi_{\rho v} \\ \psi_{\rho w} \\ \psi_{\rho E} \end{Bmatrix} = \begin{Bmatrix} \psi_\rho \\ \vec{\varphi} \\ \psi_{\rho E} \end{Bmatrix}. \quad (30)$$

To find the gradient information needed to minimize the objective function, we take the first variation of Eq. (29) with respect to perturbations of the surface shape:

$$\delta J = \int_{t_0}^{t_f} \int_S (\vec{d} \cdot \nabla p) \delta S ds dt + \int_{t_0}^{t_f} \int_S (\vec{d} \cdot \vec{n}_S) \delta p ds dt + \int_{t_0}^{t_f} \int_\Omega \Psi^T \delta \mathbf{R}(\vec{U}) d\Omega dt. \quad (31)$$

It is important to note that the first two terms of Eq. (31) are found by using a result from previous work by Palacios, et. al.² based on differential geometry formulas, and this is a key feature differentiating the current formulation from other adjoint approaches. The third term of Eq. (31) can be expanded by including the linearized version of the governing equations with respect to small perturbations of the design surface,

$$\begin{aligned} \delta \mathbf{R}(\vec{U}) &= \frac{\partial}{\partial t} (\delta \vec{U}) + \nabla \cdot \delta \vec{F} - \nabla \cdot \delta (\vec{U} \otimes \vec{u}_\Omega) \\ &= \frac{\partial}{\partial t} (\delta \vec{U}) + \nabla \cdot \left(\frac{\partial \vec{F}}{\partial \vec{U}} \delta \vec{U} \right) - \nabla \cdot \left[\frac{\partial (\vec{U} \otimes \vec{u}_\Omega)}{\partial \vec{U}} \delta \vec{U} \right] \\ &= \frac{\partial}{\partial t} (\delta \vec{U}) + \nabla \cdot \left(\vec{A} - \vec{I} \vec{u}_\Omega \right) \delta \vec{U}, \end{aligned} \quad (32)$$

along with the linearized form of the boundary condition at the surface,

$$\delta \vec{v} \cdot \vec{n}_S = -(\vec{v} - \vec{u}_\Omega) \cdot \delta \vec{n}_S - \partial_n (\vec{v} - \vec{u}_\Omega) \cdot \vec{n}_S \delta S \quad (33)$$

where \vec{A} is the Jacobian of \vec{F} using conservative variables. Eq. (33) can now be introduced into Eq. (31) to produce

$$\delta J = \int_{t_0}^{t_f} \int_S (\vec{d} \cdot \nabla p) \delta S ds dt + \int_{t_0}^{t_f} \int_S (\vec{d} \cdot \vec{n}_S) \delta p ds dt + \int_{t_0}^{t_f} \int_\Omega \Psi^T \frac{\partial}{\partial t} (\delta \vec{U}) d\Omega dt + \int_{t_0}^{t_f} \int_\Omega \Psi^T \nabla \cdot (\vec{A} - \bar{\vec{u}}_\Omega) \delta \vec{U} d\Omega dt \quad (34)$$

By removing any dependence on variations of the flow variables, δp , the variation of the objective function for multiple surface deformations can be found *without* the need for multiple flow solutions which results in a computationally efficient method for aerodynamic design involving many design variables. We now perform manipulations to remove this dependence. After changing the order of integration, integrating the third term of Eq. (34) by parts gives

$$\int_{t_0}^{t_f} \int_\Omega \Psi^T \frac{\partial}{\partial t} (\delta \vec{U}) d\Omega dt = \int_\Omega [\Psi^T \delta \vec{U}]_{t_0}^{t_f} d\Omega - \int_{t_0}^{t_f} \int_\Omega \frac{\partial \Psi^T}{\partial t} \delta \vec{U} d\Omega dt \quad (35)$$

A zero-value initial condition for the adjoint variables can be imposed, and assuming an unsteady flow, the first term on the right hand side of Eq. (35) can be eliminated with the temporal conditions below (the cost function does not depend on t_f). Referring to the trajectory above, the dynamic pressure (and hence the aerodynamic forces) will begin and end very close to zero, allowing for a zero final condition.

$$\Psi(\vec{x}, t_0) = 0, \quad (36)$$

$$\Psi(\vec{x}, t_f) = 0. \quad (37)$$

Now, integrating the fourth term of Eq. (34) yields

$$\int_{t_0}^{t_f} \int_\Omega \Psi^T \nabla \cdot (\vec{A} - \bar{\vec{u}}_\Omega) \delta \vec{U} d\Omega dt = \int_{t_0}^{t_f} \int_\Omega \nabla \cdot [\Psi^T (\vec{A} - \bar{\vec{u}}_\Omega) \delta \vec{U}] d\Omega dt - \int_{t_0}^{t_f} \int_\Omega \nabla \Psi^T \cdot (\vec{A} - \bar{\vec{u}}_\Omega) \delta \vec{U} d\Omega dt, \quad (38)$$

and applying the divergence theorem to the first term on the right hand side of Eq. (38), assuming a smooth solution, gives

$$\begin{aligned} \int_{t_0}^{t_f} \int_\Omega \nabla \cdot [\Psi^T (\vec{A} - \bar{\vec{u}}_\Omega) \delta \vec{U}] d\Omega dt &= \int_{t_0}^{t_f} \int_S \Psi^T (\vec{A} - \bar{\vec{u}}_\Omega) \cdot \vec{n}_S \delta \vec{U} ds dt \\ &\quad + \int_{t_0}^{t_f} \int_{\Gamma_\infty} \Psi^T (\vec{A} - \bar{\vec{u}}_\Omega) \cdot \vec{n}_S \delta \vec{U} ds dt \\ &\quad - \int_{t_0}^{t_f} \int_\Omega \Psi^T (\vec{A} - \bar{\vec{u}}_\Omega) \cdot \vec{n}_S \delta \vec{U} d\Omega dt. \end{aligned} \quad (39)$$

With the appropriate choice of characteristic-based boundary conditions, the integral over the far-field boundary can be forced to vanish. Combining and rearranging the results from Eqs. (34), (35), (36), (37), and (38) yields an intermediate expression for the variation of the cost function,

$$\begin{aligned} \delta J = \int_{t_0}^{t_f} \int_S (\vec{d} \cdot \nabla p) \delta S ds dt + \int_{t_0}^{t_f} \int_S (\vec{d} \cdot \vec{n}_S) \delta p ds dt + \int_{t_0}^{t_f} \int_S \Psi^T (\vec{A} - \bar{\vec{u}}_\Omega) \cdot \vec{n}_S \delta \vec{U} ds dt \\ - \int_{t_0}^{t_f} \int_\Omega \left[\frac{\partial \Psi^T}{\partial t} + \nabla \Psi^T \cdot (\vec{A} - \bar{\vec{u}}_\Omega) \right] \delta \vec{U} d\Omega dt. \end{aligned} \quad (40)$$

The final term of Eq. (40) can also be made to vanish, if its integrand is zero at every point in the domain. When set equal to zero, the terms within the brackets constitute the set of partial differential equations which are commonly referred to as the adjoint equations. Therefore, the domain integral will vanish provided that the adjoint equations are satisfied as

$$\frac{\partial \Psi^T}{\partial t} + \nabla \Psi^T \cdot (\vec{A} - \bar{\vec{I}}\vec{u}_\Omega) = 0 \quad \text{in } \Omega, \quad (41)$$

or, after taking the transpose,

$$\frac{\partial \Psi}{\partial t} + (\vec{A} - \bar{\vec{I}}\vec{u}_\Omega) \cdot \nabla \Psi = 0 \quad \text{in } \Omega. \quad (42)$$

The accompanying boundary condition will be given below. Furthermore, the surface integral in the third term on the right hand side of Eq. (40) can be evaluated given our knowledge of \vec{A} , \vec{u}_Ω , the wall boundary condition, $(\vec{v} - \vec{u}_\Omega) \cdot \vec{n}_S = 0$, and the linearized wall boundary condition in Eq. (33). By leveraging previous derivation of Economou, Palacios, et. al⁹ with some slight modifications and including time integration, it can be shown that evaluating the surface integral and rearranging the variation of the functional gives

$$\delta J = \int_{t_0}^{t_f} \int_S \left[(\vec{d} \cdot \nabla p) + (\nabla \cdot \vec{v}) v + (\vec{v} - \vec{u}_\Omega) \cdot \nabla(v) \right] \delta S ds dt + \int_{t_0}^{t_f} \int_S \left[\vec{d} \cdot \vec{n}_S - \vec{n}_S \cdot \vec{\varphi} - \psi_{\rho E}(\vec{v} \cdot \vec{n}_S) \right] \delta p ds dt, \quad (43)$$

where $v = \rho \psi_\rho + \rho \vec{v} \cdot \vec{\varphi} + \rho H \psi_{\rho E}$. Therefore, the adjoint equations with the admissible adjoint boundary condition that eliminates the dependence on the fluid flow variations (δp) by forcing the second term on the right hand side of Eq. (43) to vanish can be written as

$$\begin{aligned} \frac{\partial \Psi}{\partial t} + (\vec{A} - \bar{\vec{I}}\vec{u}_\Omega)^T \cdot \nabla \Psi &= 0 \quad \text{in } \Omega, \\ \vec{n}_S \cdot \vec{\varphi} &= \vec{d} \cdot \vec{n}_S - \psi_{\rho E}(\vec{v} \cdot \vec{n}_S) \quad \text{on } S, \end{aligned} \quad (44)$$

and the variation of the objective function becomes

$$\delta J = \int_{t_0}^{t_f} \int_S \left[(\vec{d} \cdot \nabla p) + (\nabla \cdot \vec{v}) v + (\vec{v} - \vec{u}_\Omega) \cdot \nabla(v) \right] \delta S ds dt = \int_{t_0}^{t_f} \int_S \frac{\partial J}{\partial S} \delta S ds, \quad (45)$$

where

$$\frac{\partial J}{\partial S} = \vec{d} \cdot \nabla p + (\nabla \cdot \vec{v}) v + (\vec{v} - \vec{u}_\Omega) \cdot \nabla(v) \quad (46)$$

is what we call the *surface sensitivity*. The surface sensitivity provides a measure of the variation of the objective function with respect to infinitesimal variations of the surface shape in the direction of the local surface normal. This value is computed at each surface node of the numerical grid at each physical time step with negligible computational cost. Note that the final expression for the variation involves only a surface integral at each physical time step and has no dependence on the volume mesh.

C. Application to Spherically-Parameterized Geometries

The surface sensitivity discussed in the previous section provides the sensitivity of the chosen functional to locally-normal displacements of the surface of interest. Typically, a large enough number of surface nodes is used such that using the locations of surface nodes directly as independent variables in an optimization results in an optimization problem of impractically high dimensionality. Hence, a parameterization of the geometry is used to

reduce the dimensionality via a mapping of the parameters of interest to the positions of the surface nodes. Several such mappings are available in the SU² design suite and in this work we add a spherical parameterization convenient to rocket shapes.

The sensitivity of any geometric parameter to the functional can be expressed as the sum of the dot product of the local normal vector, $\hat{\mathbf{n}}$, with the change in position of the corresponding node due to a change in the parameter, x_i , summed over the surface (N nodes, indexed by j):

$$\frac{\partial J}{\partial x_i} = \sum_{j=1}^N \frac{\partial \mathbf{r}_j}{\partial x_i} \cdot \left(\frac{\partial J}{\partial S} \hat{\mathbf{n}} \right)_j = \sum_{j=1}^N \left(\frac{\partial J}{\partial S} \right)_j \left(\frac{\partial x_j}{\partial x_i} n_x + \frac{\partial y_j}{\partial x_i} n_y + \frac{\partial z_j}{\partial x_i} n_z \right). \quad (47)$$

(Note that x in Eq. (47) is used to represent both the Cartesian coordinate as well as a specific design parameter.) SU² provides the values of dJ/dS while the values of $\partial x/\partial x_i$, $\partial y/\partial x_i$, and $\partial z/\partial x_i$ define the surface parameterization. The unit normal vector can be evaluated either from the surface mesh or analytically from the parameterization depending on the level of geometric complexity. Here the surface normal vectors are evaluated analytically from spherical geometry.

For a local spherical coordinate shown above in Fig. 2 with the axis positive forward through the nose, the Cartesian coordinates are expressed as

$$\begin{aligned} x &= r \cos(\theta) \\ y &= r \sin(\theta) \cos(\phi), \\ z &= r \sin(\theta) \sin(\phi) \end{aligned} \quad (48)$$

where r is a function of θ and ϕ . The geometry is parameterized by m control points, \mathbf{r}_i ($i = 1, \dots, m$). In order to achieve the reduction in dimensionality an interpolation scheme is required to determine r_j from the set of control points $\{\mathbf{r}_i\}$. Differentiating Eqs. (48) and substituting into Eq. (47) yields

$$\frac{\partial J}{\partial r_i} = \sum_{j=1}^N \left(\frac{\partial J}{\partial n} \right)_j \frac{\partial r_j}{\partial r_i} \left(\cos(\theta) n_x + \cos(\theta) \cos(\phi) n_y + \cos(\theta) \sin(\phi) n_z \right)_j. \quad (49)$$

Equation (50) can be used to find the sensitivity of the functional J to changes in r_i , provided an interpolation operator $\partial r_j/\partial r_i$ is available, given the location and local unit normal vector of each surface node from the adjoint surface sensitivities dJ/dS . For an axisymmetric geometry, the unit normal vectors are given by Eqs. (50),

$$\begin{aligned} n_x &= -\frac{\sin(\theta) + \tilde{r} \cos(\theta)}{\sqrt{\tilde{r}^2 + 1}}, \\ n_y &= \left(\frac{\cos(\theta) - \tilde{r} \sin(\theta)}{\sqrt{\tilde{r}^2 + 1}} \right) \cos(\phi), \\ n_z &= \left(\frac{\cos(\theta) - \tilde{r} \sin(\theta)}{\sqrt{\tilde{r}^2 + 1}} \right) \sin(\phi), \\ \tilde{r} &\equiv r \left(\frac{dr}{d\theta} \right)^{-1}. \end{aligned} \quad (50)$$

This closes the geometric system, allowing for dJ/dr_i to be evaluated via dr_j/dr_i . Any appropriate numerical method can be used to find dr_j/dr_i depending on the operator and implementation. Here, a complex step method was used to perturb each control point and evaluate dr_j/dr_i :

$$\frac{\partial r_j}{\partial r_i} = \frac{\text{Im}[r_j(r_i + \Delta r_i i)]}{\Delta r_i}. \quad (51)$$

VI. Aerodynamic Model

This section summarizes the computational fluid dynamics (CFD) model used to evaluate the aerodynamic properties of the launch via SU². Inviscid flow physics were chosen in order to reduce computational cost, the overall procedure is unchanged if viscous flow is considered. It is noted, however, that the mesh deformation method discussed above can be considerably less robust when boundary layer cells are involved. A 180° model of the fairing and a portion of the launch vehicle was created using quadrilateral surface elements and tetrahedral volume elements with a layer of pyramid elements between. A hemispherical farfield was placed approximately 30 vehicle radii away nodes were bunched near the nose and near any corners. The baseline mesh, totaling approximately 800,000 cells, is shown below in Fig. 5.

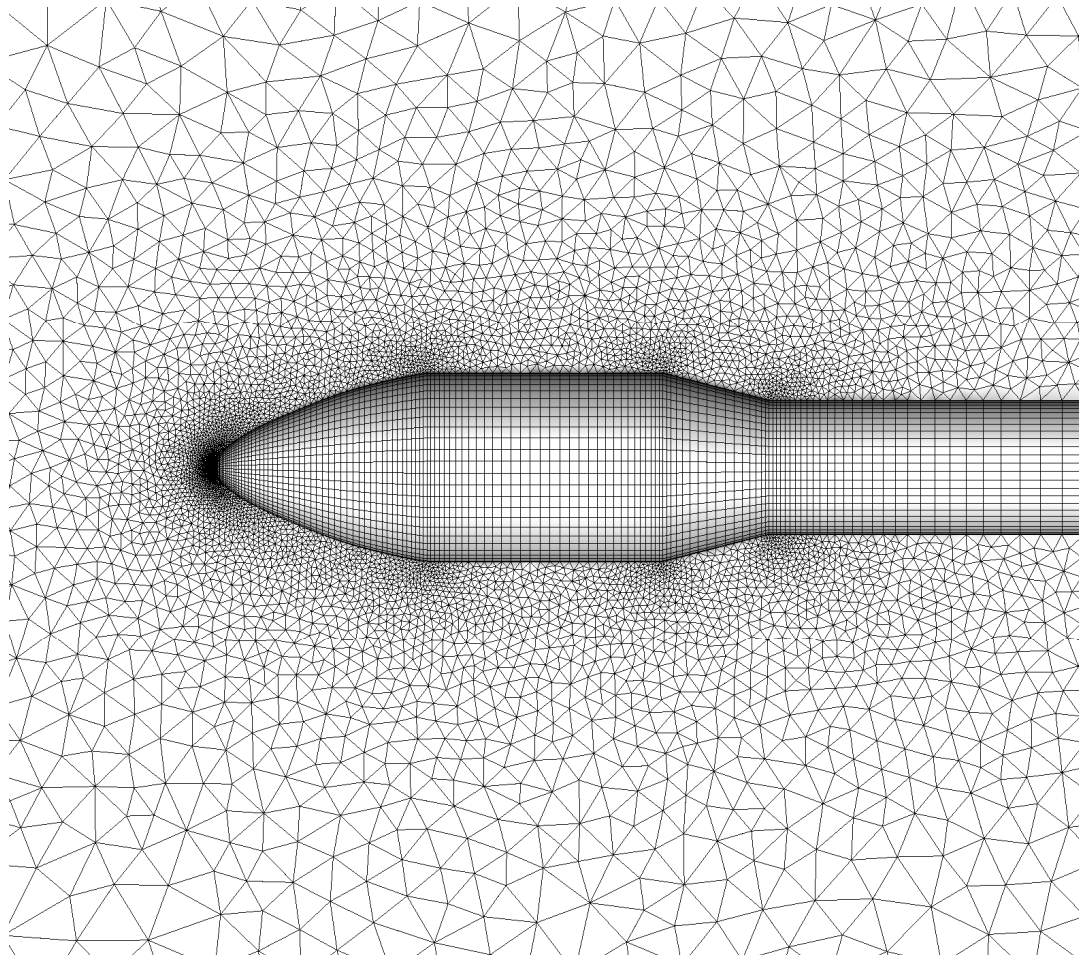


Figure 5. Inviscid CFD mesh of baseline fairing and portion of the launch vehicle showing detail near the nose of corners of the fairing profile.

VII. Optimization Procedure

This section summarizes the optimization procedure used. The procedure described above allows for a straightforward implementation of well-established optimization algorithms. The locations of the spline control points or locations and amplitude of the Hicks-Henne function are continuous variables with simple bounds and it is expected that the objective function(s) and nonlinear constraints (both of which are simple functions of the aerodynamic quantities C_A and C_M) will be smooth and continuous in the design space. Hence, standard gradient-based optimization algorithms^{10,13,16} can be used and a sequential quadratic programming (SQP) algorithm was chosen for use here to make efficient use of the gradient information provided by the adjoint sensitivities.

The SQP algorithm requires the value of the objective, J , and corresponding gradients, $\partial J / \partial \mathbf{x}$, in addition to the nonlinear constraint function(s), \mathbf{c} , and corresponding gradients, $\partial \mathbf{c} / \partial \mathbf{x}$, for a given \mathbf{x} . The specific formulation of

this optimization problem requires $C_A(\mathbf{x})$ and $m_f(\mathbf{x})$ for objective evaluation and $C_A(\mathbf{x})$, $C_M(\mathbf{x})$, and $m_f(\mathbf{x})$ for constraint evaluation. It is useful to summarize the complete process of each in the context of SU²:

Objective Evaluation:

1. Deform CFD mesh from baseline, \mathbf{x}_0 , to current value, \mathbf{x}
2. Perform a time-accurate flow solution with the deformed mesh over the trajectory
3. Process the flow solution data (surface integration) at each time step $\rightarrow C_A(t)$
4. Perform an adjoint solution of functional C_A on the deformed mesh (requires the flow solution data)
5. Project the gradients from adjoint surface data to the design variables \mathbf{x} , at each time step $\rightarrow \partial C_A(t)/\partial \mathbf{x}$
6. Integrate $C_A(t)$ and $\partial C_A(t)/\partial \mathbf{x}$ in time over the trajectory data $\rightarrow J, \partial J/\partial \mathbf{x}$

Constraint Evaluation:

1. Deform CFD mesh from baseline, \mathbf{x}_0 , to current value, \mathbf{x}
2. Perform time-accurate flow solution on deformed mesh over trajectory
3. Process flow solution data (surface integration) at each time step $\rightarrow C_A(t), C_M(t)$
4. Perform adjoint solution of functional C_A on deformed mesh (requires flow solution data)
5. Perform adjoint solution of functional C_M on deformed mesh (requires flow solution data)
6. Project gradients from adjoint surface data to design variables \mathbf{x} at each time step $\rightarrow \partial C_A(t)/\partial \mathbf{x}, \partial C_M(t)/\partial \mathbf{x}$
7. Integrate $C_A(t), \partial C_A(t)/\partial \mathbf{x}, C_M(t), \partial C_M(t)/\partial \mathbf{x}$ in time over the trajectory data $\rightarrow c, \partial c/\partial \mathbf{x}$

Of the items above, the flow and adjoint solutions required the greatest computational expense with adjoint solutions somewhat more expensive than flow solutions. Volume mesh deformation was a small but significant expense. It is noted that, due to the wide range of flow conditions and static CFD mesh (with respect to the flow features) very conservative solver settings were required throughout the entire time-accurate solution. This is discussed in more detail in the following section.

The SQP algorithm will efficiently find a local minimum. In order to improve the chances of capturing the global minimum several different values of \mathbf{x}_0 were used as initial points in addition to the baseline shown above. Initial points were “corners” of the design space, or locations were at least two geometric constraints intersected. It is noted that this procedure is heuristic and does not guarantee global minimization but has been effective method to improve coverage of the design space in previous studies⁶.

VIII. Results & Discussion

A. Baseline Vehicle

This section describes the results of a specific case used to demonstrate the method in addition to discussing future directions of research. The baseline medium-lift launch vehicle parameters used for the sample results (and to generate the trajectory data shown above) are summarized in Table 1. The fairing nose was parameterized with four spline control points, $\mathbf{x}_0 = \{6.0 \text{ m}, 5.0 \text{ m}, 4.0 \text{ m}, 3.0 \text{ m}\}$, at fixed $\theta = \{0, \pi/16, \pi/8, \pi/4\}$. Fixed θ was chosen only to reduce the problem dimensionality and hence computational expense. Recall that $r(\pi/2)$ is fixed at R_{cyl} and both ends of the spline are constrained by $\partial r/\partial \theta = 0$.

Launch Vehicle Parameters

First stage structural mass	= 13,000 kg
First stage propellant mass	= 240,000 kg
Frist stage I_{sp}	= 300 s
Second stage structural mass	= 3,600 kg
Second stage propellant mass	= 45,000 kg
Second stage I_{sp}	= 350 s
Payload Mass	= 8,000 kg
Propellant Mass at Fairing Deployment	= 43,000 kg
Reference Stress	= 275 MPa (Al 6061-T6 yield)
Reference Skin Thickness	= 2.54 mm (0.10")
Reference Vehicle Radius	= 1.85 m
Fairing Cylinder Radius	= 2.60 m

Fairing Surface Mass Density	= 11 kg/m ² (general carbon / Al composite)
Limit C_{load}	= 0.100
Ideal Vehicle ΔV ($m_f = 0$, $C_A = 0$)	= 9.596 km/s

Table 1. Summary of launch vehicle parameters required for fairing optimization.

The baseline vehicle and fairing yielded the performance summarized in Table 2. Flow and adjoint contour plots corresponding to the baseline design are shown in Fig. 6 and Figs. 7-10, respectively.

\mathbf{x}_0	= {6.0 m, 5.0 m, 4.0 m, 3.0 m}, $\theta = \{0, \pi/16, \pi/8, \pi/4\}$
Total Vehicle ΔV	= 9.466 km/s
Fairing Mass	= 2,381 kg
C_{load}	= 0.0986

Table 2. Summary of launch vehicle parameters required for fairing optimization.

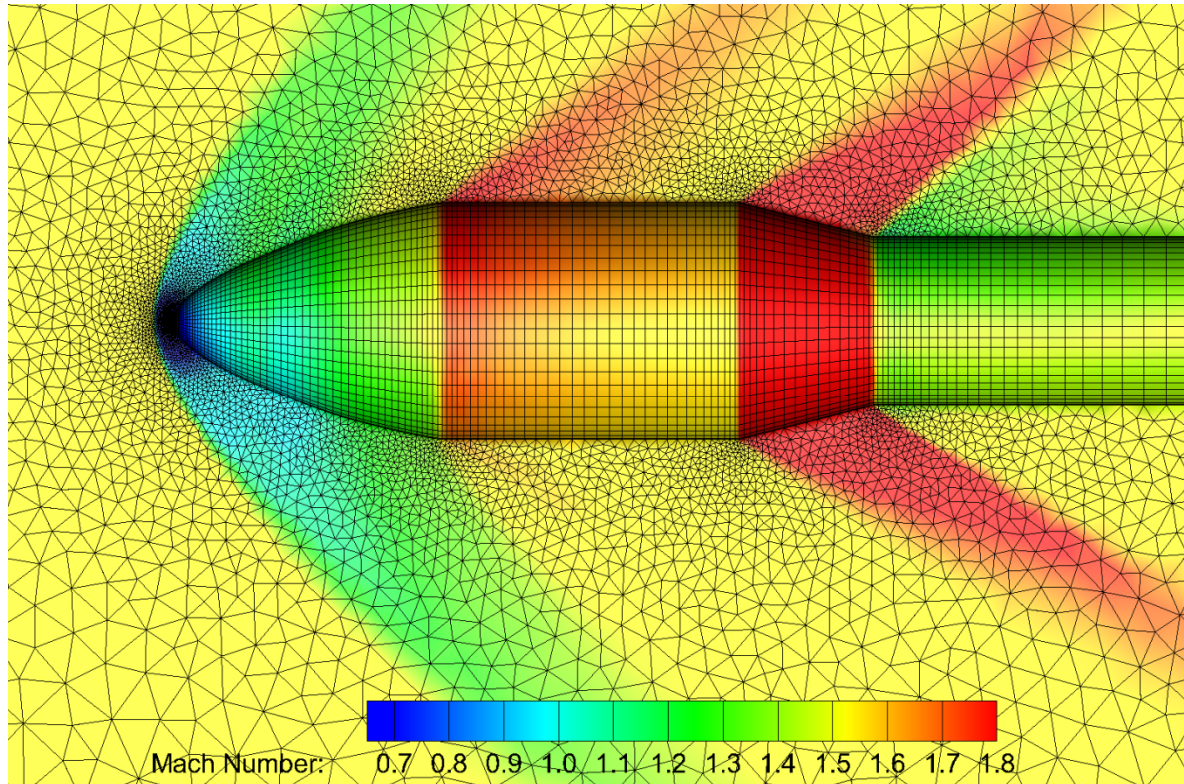


Figure 6. Mach contours for the baseline design under maximum q_∞ conditions and $\alpha = 5.0^\circ$.

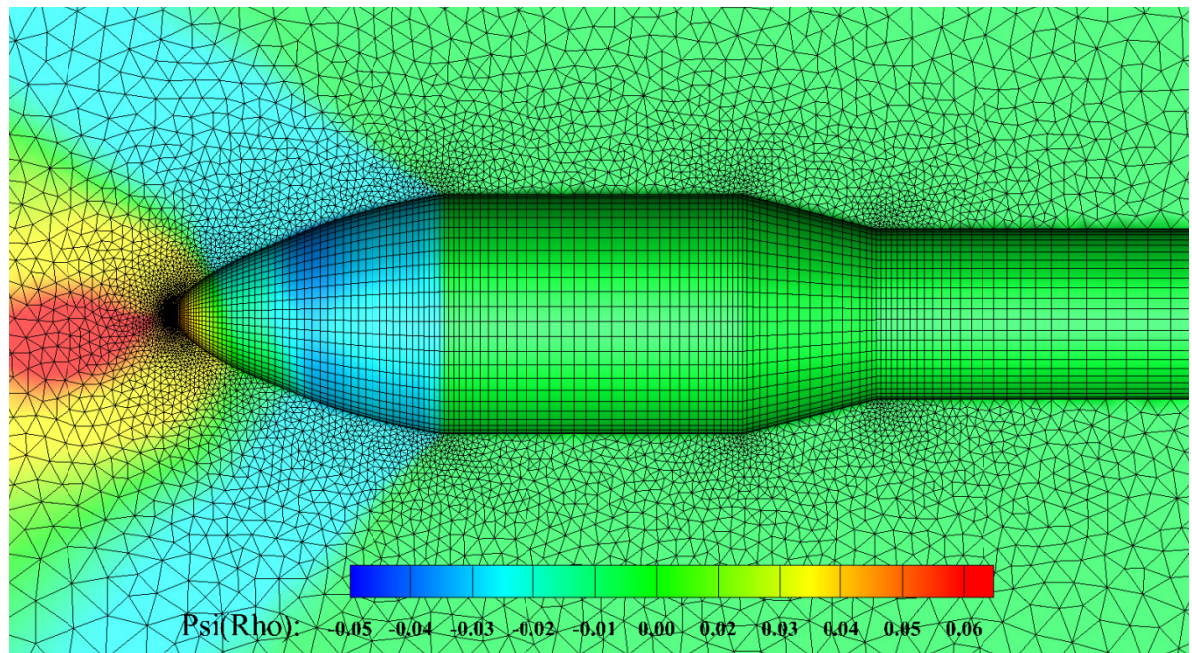


Figure 7. Ψ_ρ contours for the baseline design under maximum q_∞ conditions and $\alpha = 5.0^\circ$ for functional C_A .

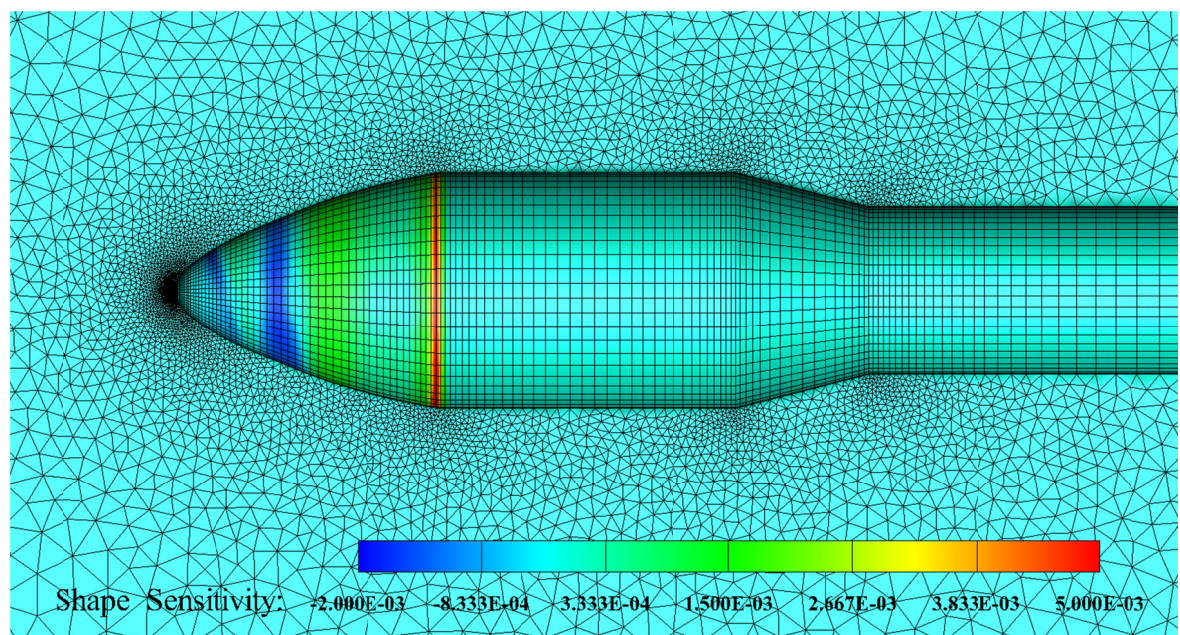


Figure 8. Shape sensitivity ($\partial J / \partial S$) contours for the baseline design under maximum q_∞ conditions and $\alpha = 5.0^\circ$ for functional C_A .

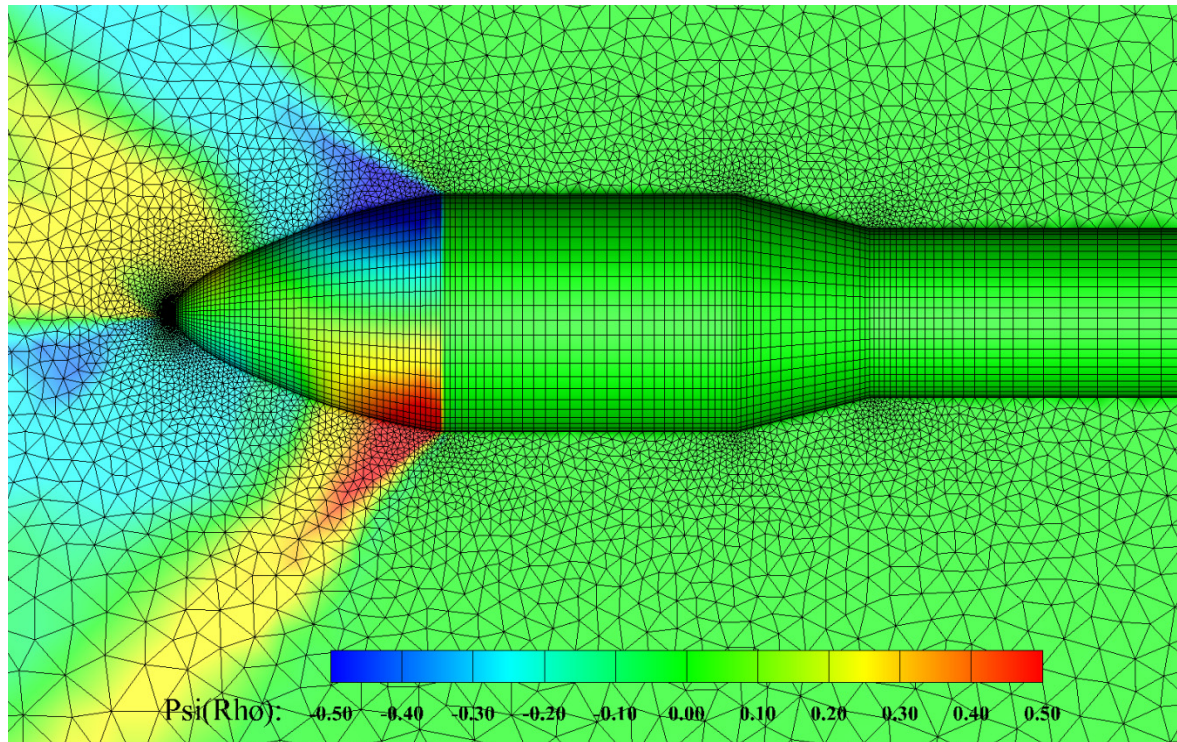


Figure 9. Ψ_ρ contours for the baseline design under maximum q_∞ conditions and $\alpha = 5.0^\circ$ for functional C_M .

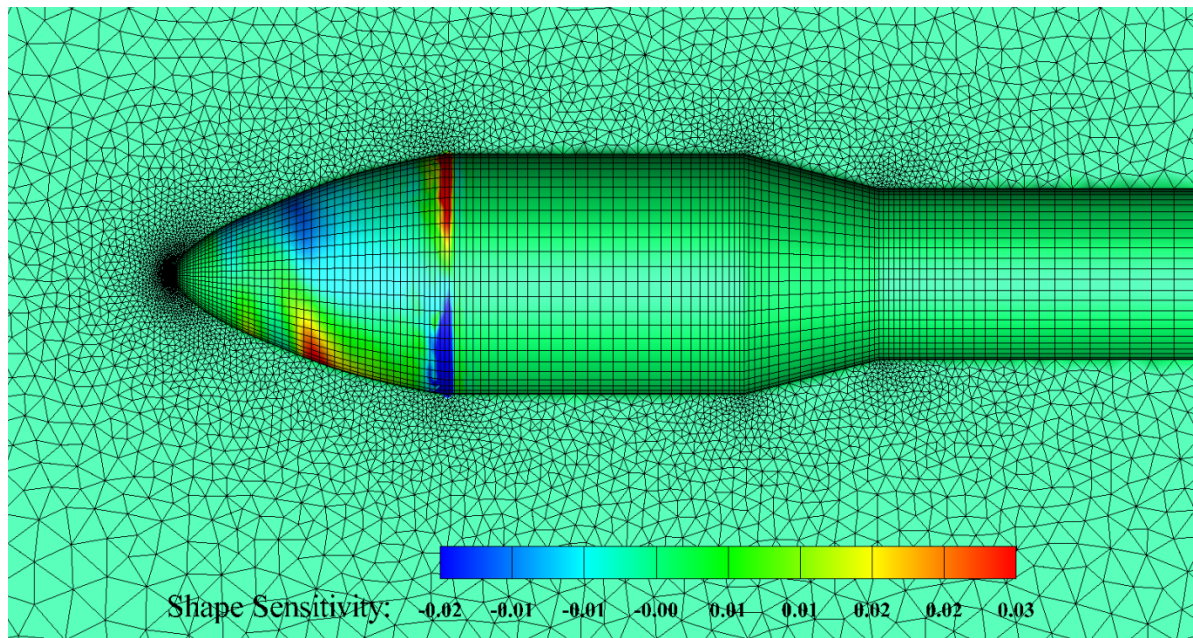


Figure 10. Shape sensitivity ($\partial J / \partial S$) contours for the baseline design under maximum q_∞ conditions and $\alpha = 5.0^\circ$ for functional C_M .

B. Optimum Design

Qualitatively, the optimization procedure is a balance between the conflicting effects of geometry on mass (surface area) and drag. Minimizing the mass of the fairing will tend to shorten it and move the profile inward toward the axis to reduce the surface area. Minimizing the drag alone results in a longer profile with higher L/R but also larger surface area. The drag (more specifically C_A) is shared by both the objective function and the structural

constraint, though in the formulation of the constraint, Eq. (9), the bending moment is emphasized. Based on this intuition and the form of the surface sensitivity contours with respect to J we should expect an optimum shape that reduces $r(\theta)$ everywhere possible until the drag penalty incurred becomes too large. The length of the fairing (r at the nose) may increase or decrease depending on the trade between mass and drag. The optimal profile is shown below in Fig. 11.

Optimum Design

\mathbf{x}^*	= {6.2871 m, 4.5578 m, 3.4071 m, 2.7479 m}, $\theta = \{0, \pi/16, \pi/8, \pi/4\}$
Total Vehicle ΔV	= 9.501 km/s
Fairing Mass	= 2,307 kg
C_{load}	= 0.08655

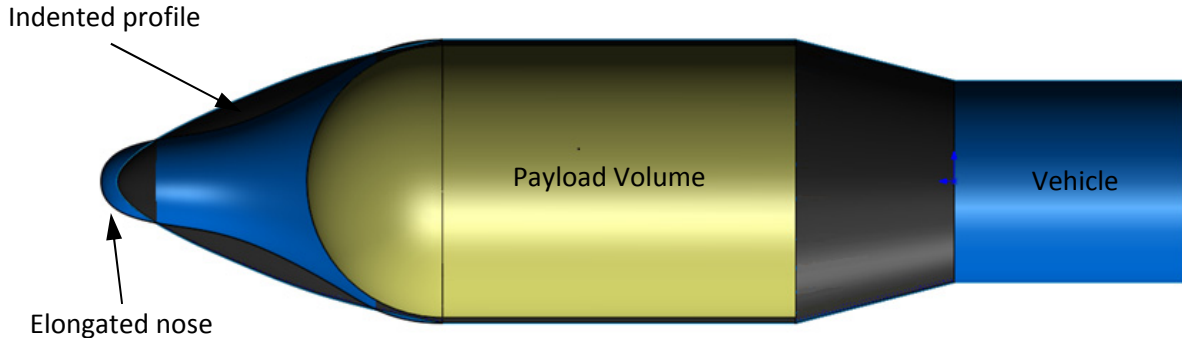


Figure 11. Cross-sectional view of an optimum design (blue) vs. the baseline design (black). Note the “pinched” shape of the fairing which reduces the fairing’s mass while maintaining comparable aerodynamic performance at higher M_∞ .

It is worth noting that the profile above actually causes a performance reduction (larger C_A but lower mass) when analyzed only at the maximum q_∞ condition. This underscores the need to simulate over the entire atmospheric portion of the ascent trajectory as the optimum profile has superior performance for much of the flight after maximum q_∞ ($M_\infty > 1.5$). At high M_∞ the more-pointed nose acts like a “sting” while the rest of the surface experiences flow behind an oblique shock. This reduces the sensitivity of the rest of the surface geometry and allows $r(\theta)$ to move toward the axis and save mass. In addition, it is noted that that value of the constraint, C_{load} , actually decreased from its nominal value in the optimum design.

C. Improvements & Future Directions

Of the many steps listed above required to evaluate a given design and its corresponding gradients, the combination of grid deformation CFD solutions (flow and adjoint) are currently the least robust. The extreme nature of the flight regime results in a high sensitivity of convergence to grid quality, especially near the nose at high M_∞ . the spring-analogy solver, while generally very robust, eventually creates cells which are more skewed than those of the original mesh as \mathbf{x} moves away from \mathbf{x}_0 . Hence, at some points in the overall procedure above, an intermediate \mathbf{x}^* was re-meshed to reset the grid deformation range. Were viscous flow physics used, this issue would be exacerbated. Finally, gradient-based algorithms like SQP are generally not robust against objective or constraint functions that cannot be evaluated or yield inaccurate results (practically, flow or adjoint solutions which do not converge properly).

This procedure can hence be improved in a number of ways. First, the use a more tolerant optimization algorithm, such as particle swarm optimization, may be able to tolerate \mathbf{x} at which results are unavailable or of poor accuracy (at the likely expense of more function evaluations). Second, a more robust grid deformation algorithm would increase the range of \mathbf{x} over which designs could be accurately evaluated. As of this writing, an elasticity-based grid deformation capability is nearing completion in the SU² suite and will be utilized in future studies. In addition, modifying the flow and adjoint solution algorithm to allow for settings which are a function of the free stream conditions would accelerate convergence performance while safeguarding conditions at which conservative settings are required. This improvement is also expected in SU² and will be utilized in future studies.

Finally, the optimization problem as formulated here is merely a subset of a larger MDO problem as discussed above. Some of the neglected dependencies, including the fairing's effect on the trajectory near maximum q_∞ and the sensitivity of the launch vehicle's structural mass to the loads applied by the fairing, are likely comparable in effect to those studied here. Bringing the trajectory calculation and a structural analysis – even a relatively simple or low-fidelity one – into the optimization loop would improve the completeness of the results without adding substantially to the overall computational cost.

References

- ¹Blades, E. L., and Newman, J. C., III, "Computational-Fluid-Dynamics-Based Design Optimization of a Large Asymmetric Payload Fairing," *AIAA Journal of Spacecraft and Rockets*, accepted for publication, 2013. doi: 10.2514/1.A32301.
- ²Bueno-Orovio, A., Castro, C., Palacios, F., and Zuazua, E., "Continuous Adjoint Approach for the Spalart-Allmaras Model in Aerodynamic Optimization", *AIAA Journal*, Vol. 50, No. 3, pp. 631-646, March 2012.
- ³Braun, R. D., Moore, A. A., and Kroo, I. M., "Collaborative Approach to Launch Vehicle Design", *Journal of Spacecraft and Rockets*, Vol. 34 No. 4, July-August 1997.
- ⁴Braun, R. D., Powell, R. W., Lepsch, R. A., Stanley, D. O., and Kroo, I. M., "Comparison of Two Multidisciplinary Optimization Strategies for Launch-Vehicle Design", *Journal of Spacecraft and Rockets*, Vol. 32 No. 3, May-June 1995.
- ⁵Brown, N. F. and Olds, J. R., "Evaluation of Multidisciplinary Optimization (MDO) Techniques Applied to a Reusable Launch Vehicle", 43rd AIAA Aerospace Sciences Meeting and Exhibit, January 2005.
- ⁶Colonna, M. R., *A Multidisciplinary Optimization Environment for Rocket Vehicle Systems*, Ph.D. thesis, Stanford University, 2007.
- ⁷Colonna, M. R. and Alonso, J. J., "The Optimum Launch Vehicle Fairing: an MDO Approach", 12th AIAA Multidisciplinary Analysis and Optimization Conference, Victoria, BC, September, 2008.
- ⁸Degand, C. and Farhat, C., "A Three-dimensional Torsional Spring Analogy Method for Unstructured Dynamic Meshes," *Computers & Structures*, Vol. 80, pp. 305-316, 2002.
- ⁹Economou, T. D., Palacios, F., Alonso, J. J., "Optimal Shape Design for Open Rotor Blades", 30th AIAA Applied Aerodynamics Conference, New Orleans, LA, June, 2012.
- ¹⁰Gill, P. E., Murray, W., and Saunders, M. A., "SNOPT: An SQP Algorithm for Large-Scale Constrained Optimization," *SIAM Review*, Vol. 47, No. 1, 2005, pp. 99-131.
- ¹¹Guruswamy, G. P. and Obayashi, S., "Use of High-Fidelity Methods in Multidisciplinary Optimization – A Preliminary Survey", 9th AIAA / ISSMO Multidisciplinary Analysis and Optimization Conference, September 2002.
- ¹²Guruswamy, G. P. and Obayashi, S., "Study on the Use of High-Fidelity Methods in Aeroelastic Optimization", *Journal of Aircraft*, Vol. 41 No. 3, 2004.
- ¹³Han, S. P., "A Globally Convergent Method for Nonlinear Programming," Vol. 22, *Journal of Optimization Theory and Applications*, p. 297, 1977.
- ¹⁴Hicks, R. M., Murman, E. M., and Vanderplaats, G. N., "An Assessment of Airfoil Design by Numerical Optimization", NASA TM X-3092, NASA, July 1974.
- ¹⁵Jameson, A., "Aerodynamic Design via Control Theory", *Journal of Scientific Computing*, 3:233-260, 1988.
- ¹⁶Jones, D. R., Schonlau, M., and Welch, W.J., "Efficient Global Optimization of Expensive Black-Box Functions", *Journal of Global Optimization*, Vol. 13, No. 4, pp. 455-492, December 1998.
- ¹⁷Knight, F. L. (Ed.), "Evolved Expendable Launch Vehicle Standard Interface Specification," Version 4.1, January 1998.
- ¹⁸Leoviriyakit, K., and Jameson, A., "Aero-structural Wing Planform Optimization," 42nd Aerospace Science Meetings & Exhibit, Reno, NV, Jan. 2004.
- ¹⁹Martins, J. R. R. A., "A Coupled-Adjoint Method for High-Fidelity Aero-Structural Optimization", Ph.D Dissertation, Department of Aeronautics and Astronautics, Stanford University, Stanford, CA, Oct. 2002.
- ²⁰Palacios, F., Alonso, J. J., Duraisamy, K., Colonna, M., Hicken, J., Aranake, A., Campos, A., Copeland, S., Economou, T. D., Lonkar, A., Lukaczyk, T., Taylor, T., "Stanford University Unstructured (SU2): An Open Source Integrated Computational Environment for Multiphysics Simulation and Design," 51st AIAA Aerospace Sciences Meeting, Grapevine, TX, Jan. 2013.
- ²¹Reuther, J. J., Jameson, A., Alonso, J. J., Rimlinger, M., and Saunders, D., "Constrained Multipoint Aerodynamic Shape Optimization Using an Adjoint Formulation and Parallel Computers: Part I & II", *Journal of Aircraft*, 36(1):51-74, 1999.
- ²²Stanford University Unstructured (SU2): <http://su2.stanford.edu>.
- ²³United Launch Alliance (ULA), "Delta II payload Planners Guide", December, 2006.
- ²⁴US Air Force Space Command, "Operational Requirements Document for the Evolved Expendable Launch Vehicle", AFSPSC 002-93-I, 1 August 1995.
- ²⁵Wu, H.-Y., Yang, S., Liu, F., and Tsai, H.-M., Comparison of Three Geometric Representations of Airfoils for Aerodynamic Optimization, AIAA 2003-4095, January 2003.